Mechanical Analysis of Lithium-Ion Batteries Via Acoustic Impedance Spectroscopy

Charles Soulen, Stewart Sherrit, Erik Brandon, and Ping Liu*

Cite This: https://doi.org/10.1021/acselectrochem.4c00105

Read Online

ACCESS | Metrics & More | Article Recommendations | Supporting Information

ABSTRACT: The mechanical properties of lithium-ion batteries (LIB) are closely related to their state-of-charge (SOC) and state-of-health (SOH). Here, we introduce an in-operando acoustic technique based on acoustic impedance spectroscopy (AIS) which probes the mechanical changes that occur in the LIB during operation. Using thin, inexpensive piezoelectric resonators and widely available impedance analyzers, we can identify the acoustic resonances of commercial LIBs by measuring the complex electrical impedance of the resonator. In-operando AIS shows that these resonances are dependent on the bulk mechanical properties of the LIB, which change reversibly as the cell is cycled. We show that this technique can provide substantial information on both the SOC and SOH of a commercial LIB.

KEYWORDS: Batteries, acoustic characterization, state-of-charge, state-of-health, acoustic impedance spectroscopy
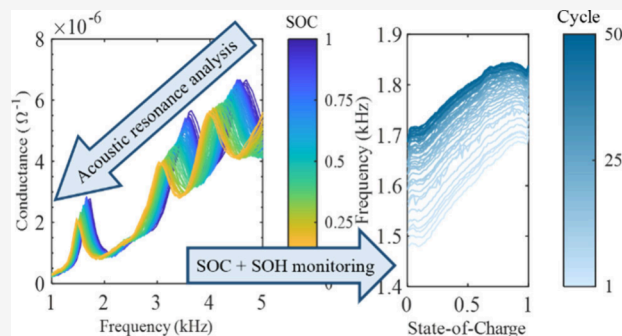
INTRODUCTION

Lithium-ion batteries (LIB) have become ubiquitous in society. During their operation, there is a coupling between the electrochemical processes used to store energy and the changes in the mechanical properties of the cell components that necessarily arise therein.[1] The electrochemical reactions that store Li in the electrodes of the LIB cause phase changes in the anode and cathode particles, resulting in variations to the LIB's mechanical properties such as Young's modulus, density, and particle volume.[2,3] Unsurprisingly, a wide variety of characterization techniques have been developed to study the coupling between the electrochemical reactions and the mechanical properties in LIBs.[4−6] Of the most useful are in-operando techniques, which can track this coupling during cycling. Understanding these changes enables the characterization of battery state-of-charge (SOC) and state-of-health (SOH), where SOH is defined as the ratio of the nth cycle capacity to the first cycle capacity. These metrics in turn are crucial for battery diagnostics, control, and life prediction.

Recently, acoustic techniques have been used to probe the mechanical properties of LIBs.[4,7,8] Ultrasonic time-of-flight (UToF) has emerged as a useful probe in both academic and commercial settings. In academic settings, UToF has been used to monitor critical properties such as solid-electrolyte interface (SEI) growth[9] and effective cell stiffness.[10] In commercial settings, UToF has been used to improve SOC and SOH estimates in LIBs.[2,11] Since the mechanical properties and the SOC are both dependent on the concentration of Li in each electrode, they are inherently linked. The success of UToF has

therefore created a desire for similar acoustic characterization techniques to compliment UToF.

In this work, we introduce an in-operando bulk acoustic characterization technique based on acoustic impedance spectroscopy (AIS). Using AIS, we measure the acoustic resonances of an LIB via the impedance spectrum of a piezoelectric resonator attached to a battery. We show that the acoustic resonances are proportional to the acoustic velocity, which allows us to track the mechanical properties (e.g. elastic modulus and density) of the LIB during cycling. We can also use this relation to validate our technique against UToF. The sensors used in AIS are inexpensive, have a low profile, and are simple to use. Moreover, they are available in a variety of shapes, sizes, and materials, and can be engineered to fit LIBs of different formats (e.g., pouch, prismatic, and cylindrical). The only instruments used in AIS are common impedance analyzers, which are already present in most academic battery laboratories and are being investigated and miniaturized for use in battery management systems (BMS).[12] In this initial study, we chose to examine three resonances of a commercial graphite-LiCoO₂ LIB pouch cell as functions of both SOC and SOH. This system has been extensively studied using UToF,
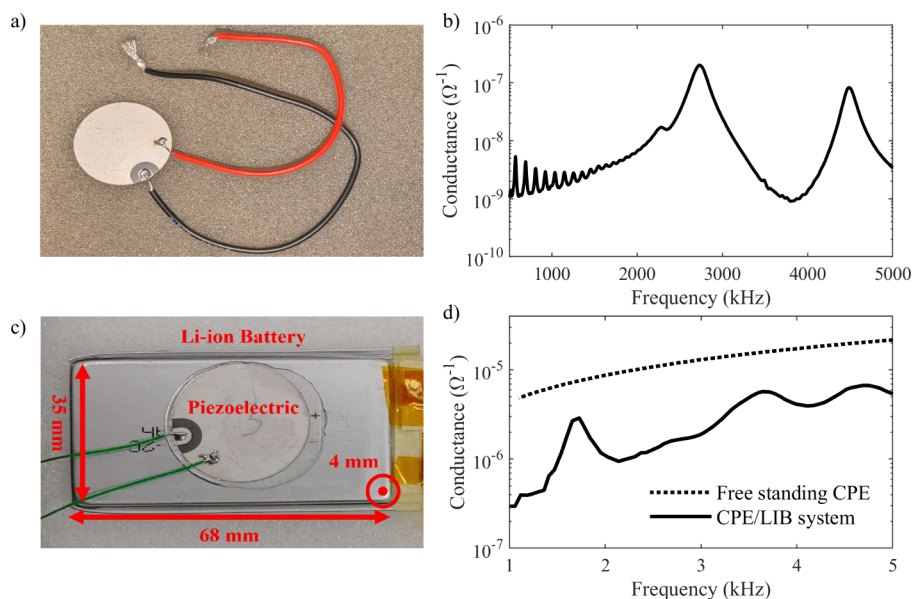
Figure 1. (a) An optical image of a CPE. Electrodes are patterned on the top and bottom of the CPE and a wrap-around lead is used. The dimensions of the CPE are 25.4 mm × 0.5 mm. (b) The AIS spectra of the CPE shown in panel a. Lower frequency peaks between 500 and 2000 kHz are the radial resonances of the CPE. The higher frequency peaks at 2750 and 4500 kHz are the first and second order thickness resonances of the CPE. (c) An optical image of the CPE/LIB system. The dimensions of the LIB are 68 mm × 35 mm × 4 mm. (b) The difference in the AIS spectrum of a free-standing CPE (dotted line) and the CPE/LIB system (solid line). The free-standing CPE has no obvious resonances in this range and thus responds as a simple capacitor. The CPE/LIB system shows multiple peaks, which are associated with the resonances of the LIB.

giving us a strong basis to compare our results against.[2,4,11] Using a correlation coefficient known as mutual information, we show that the three resonances have the potential to provide more information about the SOC than voltage measurements alone. Similarly, we show that these resonances provide substantial information on SOH. This technique would therefore complement voltage and impedance data in a commercial BMS.

EXPERIMENTAL SECTION

Acoustic Impedance Spectroscopy. AIS was conducted on commercial 800 mAh graphite/LiCoO$_2$ Li-ion batteries with dimensions 68 mm × 35 mm x 4 mm (PL-383562-2C; AA Portable Power Corp.). A commercial 25.4 mm diameter, 0.5 mm thick Pb(Zr$_x$Ti$_{1-x}$)O$_3$ (PZT-880 NAVY III) piezoelectric disc (APC International) was used as an acoustic sensor. The piezoelectric disc was patterned with wrap-around electrodes, allowing electrical leads to be connected to only one side of the disc, leaving the other side free to couple to the LIB. The disc was attached to the surface of the LIB using a DEVCON 5 min epoxy resin and allowed to dry for 24 h prior to testing. Since AIS is sensitive to the geometry of the system, asymmetries can produce additional resonances, which can complicate the measurement. Therefore, to produce the cleanest spectra, the disc was placed at the center of the LIB. Two factors determine the quality of the coupling of the piezoelectric resonator to the LIB: the mechanical Q of the LIB and the proximity of the LIB resonances to the resonances of the piezoelectric resonator. The piezoelectric resonators used in this study were chosen as a compromise between availability, cost, and coupling quality. Moreover, the piezoelectric resonators have a large electromechanical coupling coefficient, which improves the overall efficiency and sensitivity of the system.

A Gamry Instruments Interface 1000E potentiostat was used to measure the acoustic impedance of the system over a given frequency range using a 2 V peak-to-peak sinusoidal input. The time required for each AIS scan depends on the point density and frequency range. For our purposes, each AIS scan lasts approximately 5 min. Custom scripts were written in both the Gamry codebase, Explain, and MATLAB (MathWorks) to collect and process these data. Each of the chosen resonances was fitted with eq 4 and the peak frequency was extracted.

Electrochemical Cycling. LIBs were cycled in a voltage window of 2.8−4.2 V on a Landt battery cycler. A constant current, constant voltage protocol was used, wherein cells were charged to 4.2 V then pinned at 4.2 V until the current dropped below C/100 (8 mA). Cells were then discharged to 2.8 V. For most experiments, a C/10 (80 mA) rate was used. For the high rate, high temperature stress test, a rate of 1C (800 mA) was used. All cells were cycled in ESPEC temperature chambers set at 25°C for the standard test, and 45°C for the stress test.

RESULTS

Major Resonances and Their Structures. AIS is a method of determining the acoustic resonances of a system by measuring the complex electrical impedance of the system over a frequency range. Figure 1a shows a ceramic piezoelectric (CPE) disc with a diameter of 25.4 mm and a thickness 0.5 mm. The CPE has electrodes attached to either side. When a sinusoidal electrical signal is applied across the CPE it vibrates due to the high electromechanical coupling constant of the CPE. At certain frequencies, defined by the geometry and electromechanical properties of the CPE, it will resonate, resulting in a spike in both the vibrational amplitude and the complex electrical admittance Y (inverse of impedance) of the CPE.[13] The AIS spectrum of the CPE disc is shown in Figure 1b. Clear resonance peaks can be seen across the spectrum,

with the smaller, lower frequency resonance peaks representing resonances along the radial direction,[14,15] and the two larger, higher frequency resonance peaks representing resonances along the thickness direction.

To measure the acoustic resonances of a LIB we attached an identical CPE to the case of a LIB (68 mm × 35 mm × 4 mm) using a standard epoxy (Figure 1c). Using classical plate theory, we can relate the resonance frequencies of the LIB to its geometry and mechanical properties:[16]

$$f_{mn} = \frac{h}{2\pi} \sqrt{\frac{E}{\rho}} \sqrt{\frac{1}{12(1-\nu^2)}} \left[\left(\frac{m\pi}{a}\right)^2 + \left(\frac{n\pi}{b}\right)^2 \right] \quad (1)$$

Where f_{mn} is the resonance frequency, E is the Young's modulus, h is the plate thickness, ρ is the plate density, ν is the Poisson's ratio, a and b are the length and width, and m and n are the x and y mode numbers. Knowing that the acoustic velocity is equal to the square root of the Young's modulus divided by the density ($v = \sqrt{\frac{E}{\rho}}$), we can rewrite eq 1 such that f_{mn} is proportional to v:

$$f_{mn} = v \frac{h}{2\pi} \sqrt{\frac{1}{12(1-\nu^2)}} \left[\left(\frac{m\pi}{a}\right)^2 + \left(\frac{n\pi}{b}\right)^2 \right] \quad (2)$$

Using data from UToF literature, we can estimate the bulk acoustic velocity in an LIB at 100% SOC to be 900 m/s[11,17] and the Poisson's ratio to be 0.3.[2,17,18] We can then use eq 2 to calculate the first six resonance frequencies of the LIB, shown in Table 1. Based on these calculations, we choose to target the first three resonance frequencies and set our scan range to 1−5 kHz.

Table 1. First Six Resonance Frequencies of a 68 mm × 35 mm × 4 mm LIB Using eq 2[a]

m	n	f_{res} (kHz)
1	1	1767
2	1	2877
3	1	4727
1	2	5957
1	3	12942
2	2	7068

[a]An acoustic velocity of 900 m/s and a Poisson's ratio of 0.3 are used.[2,11,17].

Figure 1d shows the AIS spectra of a free-standing CPE (dashed line) and the spectra of a CPE epoxied to a LIB (solid line) within this range. In the case of the free-standing CPE, no pronounced peaks are seen. With the manufacturer-provided values for the planar frequency constant, N_p, and the diameter, D, (2300 Hz-m and 0.0254 m, respectively) we can estimate the fundamental resonance frequency of the CPE in the radial mode using

$$f_n = \frac{N_p}{D} \quad (3)$$

The estimated first order resonance ($n = 1$) for the resonance frequency is 90.6 kHz, which is well above the chosen frequency range. The CPE/LIB system shows three clear peaks in this frequency range, located at 1.6 kHz, 3.6 kHz, and 4.6 kHz. We assign these resonances to the LIB, making them representative of the mechanical properties of the LIB in

accordance with eq 1. The main difference between the three resonances is that they each have unique mode numbers (m, n in eq 1).

To investigate the low frequency resonance modes in the composite CPE/LIB structure we used laser Doppler vibrometry (LDV) to directly measure the vibrations that occur at the chosen resonances. LDV measures the out-of-plane velocity of a vibration using a laser and the Doppler effect.[19] By collecting vibrational velocity data across a grid (Figure 2a) we reconstructed images of the resonance
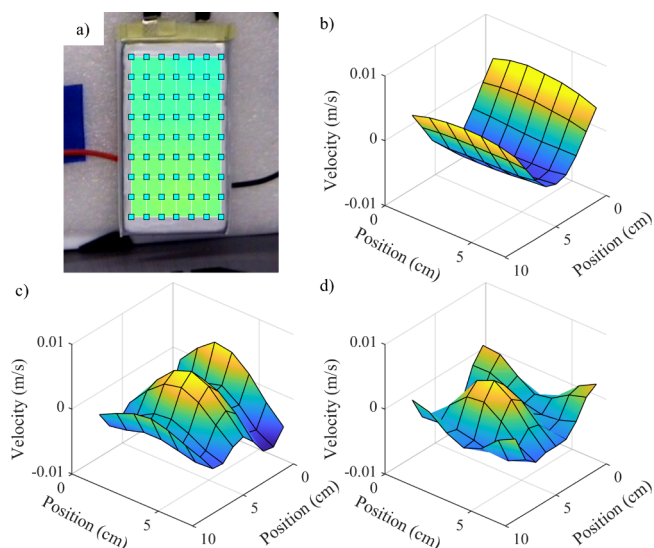

Figure 2. (a) an optical image of the LIB with the measurement locations overlaid on top. (b−d) the resonance mode shapes of the 1.6 kHz, 3.6 kHz, and 4.6 kHz, respectively. Videos of all three resonances can be found in Supplementary Videos 1−3.

structures at each frequency. Figures 2b−d show the resonance shapes for the 1.6 kHz, 3.6 kHz, and 4.6 kHz resonances, which can be clearly identified as a first order bending mode, a second order bending mode, and a first order drum mode, respectively. Videos of these resonances can be seen in Supplementary Videos 1−3.

Effects of Discharge on AIS. During discharge of an LIB, Li⁺ ions deintercalate from the anode and intercalate into the cathode. This electrochemical mass transfer alters the bulk density and Young's modulus of these materials. These effects have been reported extensively in other acoustic techniques.[2,4,20,21] To test whether AIS can track these changes, we conducted in-operando AIS while discharging the cell. Figure 3a shows the voltage curve of the cell and Figure 3b shows each spectrum taken. The 1.6 kHz, 3.6 kHz, and 4.6 kHz resonances shift to lower frequencies by 12.7%, 15.9%, and 13.7%, respectively.

The change in the acoustic resonance frequencies during discharge has also been studied using a finite element model in COMSOL Multiphysics with the parameters listed in Table S1.[22] To reduce computational expense, only a single layer of the internal repeating structure of the LIB (Al current collector/cathode/separator/anode/Cu current collector) was modeled. The first resonance of the model was compared to experiment by normalizing both values to the resonance frequency at 100% SOC. In experiment, the 1.6 kHz resonance shifts to lower frequencies by 12.7% during discharge, while the model shifts to lower frequencies by 13.8%.
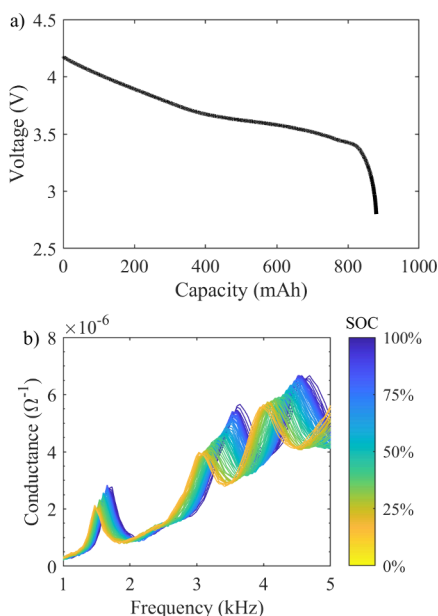
Figure 3. In-operando AIS during discharge of the LIB. (a) the voltage discharge curve of the LIB and (b) the evolution of the AIS spectrum during discharge. All three resonance peaks shift monotonically to lower frequencies during discharge.

Finally, these data can be compared against UToF. In UToF, the acoustic velocity, which is inversely proportional to the time-of-flight, is found to decrease with decreasing SOC.[10,11,23] In our data, the acoustic velocity, which is directly proportional to the resonance frequencies (eq 2) is found to decrease with decreasing SOC. Thus, given the mathematical and computational support and similarities between UToF and AIS data, we ascribe the changes to the acoustic resonance frequencies to the mechanical changes that occur in the anode and cathode during lithiation and delithiation.

The peak height of each resonance also drops significantly during discharge. The peak height is primarily dependent on the mechanical Q of the LIB, which is related to the acoustic damping in the LIB. However, the measured conductance is the sum of the conductance of the LIB and the CPE. Figure 1d shows that the conductance of the CPE changes significantly over this frequency range. Therefore, the drop in peak conductance seen in Figure 3b may be due to either the mechanical Q changing, or the resonance peaks shifting along the underlying conductance of the CPE. For simplicity, we choose to focus on the resonance frequency since this can be directly related to the acoustic velocity.

To track the frequencies of each resonance during cycling, we used eq 4 to fit each resonance and extracted the peak frequency:

$$Z_i(\omega) = \frac{1}{i\omega C_i}\left[1 - \frac{K_i^2 \tan\left(\frac{\omega}{4f_{pi}}\right)}{\frac{\omega}{4f_{pi}}}\right]$$

(4)

Where $Z_i(\omega)$ is the effective complex impedance of the ith peak, ω is the angular frequency, C_i is a complex capacitance, K_i is a complex electromechanical coupling constant, and f_{pi} is the effective complex parallel resonance frequency. All constants in bold have a real and an imaginary component.

This equation has the same mathematical form as the thickness extensional mode of a thin plate as discussed in the IEEE standard and is used extensively in previously published work.[24−26] The thickness extensional mode equation is derived from the linear equations of piezoelectricity, assuming small fields and frictionless surfaces, and is comprised of the system's capacitance multiplied by the electromechanical resonances of the system.[27] eq 4 can be used to empirically monitor weakly coupled piezoelectric resonances ($k_i < 0.3$; $k_i^2 \cong \frac{\pi^2}{4}\frac{f_P f_S - f_S^2}{f_P^2}$), such as those in our system, as it properly tracks both the resonance and antiresonance resonance frequencies in the complex impedance and admittance data. This equation can be used to track the system's resonances because the battery primarily affects only the acoustic port of the piezoelectric and has limited effect on the capacitance or electromechanical properties.

For every spectra a least squares fitting routine using a Levenberg−Marquardt algorithm was implemented to fit the C_i, K_i, and f_{pi} coefficients. It was noted that the change in the C_i, K_i, values was small compared to the f_{pi} value. The R^2 values between the fit and the data were calculated and found to typically be around 0.98. The R^2 values for the real portion, which is where the peak values were determined, was above 0.95. This equation provides a higher quality fit for our data (Figure S2) compared to generic polynomial and Gaussian fits and allows us to extract the exact resonance frequencies of the system.

Using the extracted peak frequencies, we can examine the reversibility of the spectral evolution seen in Figure 3. Figure 4 shows the peak frequencies of the three chosen resonances over 100 h of cycling at C/10 and 25°C. In all cases, the resonances show repeatability and reversibility, with all peaks increasing in frequency during charge and decreasing in frequency during discharge. This is in line with the expected
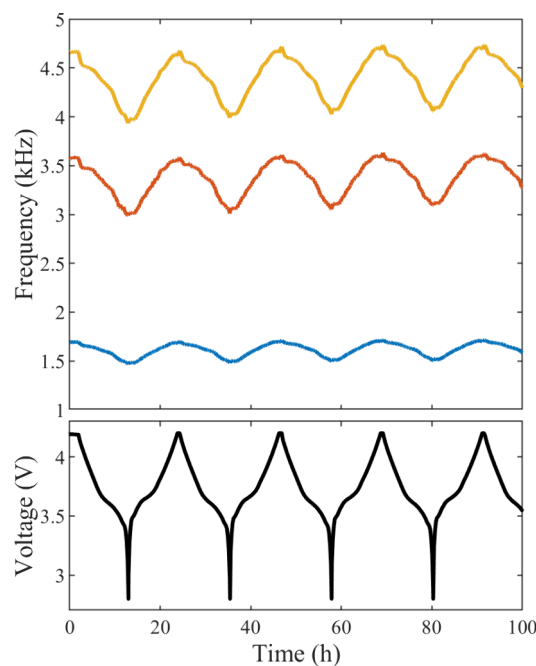

Figure 4. Evolution of the peak frequencies for the first 100 h of cycling of the 1.6 kHz, 3.6 kHz, and 4.6 kHz. The 1.6 kHz, 3.6 kHz, and 4.6 kHz peaks all have similar monotonic trends.
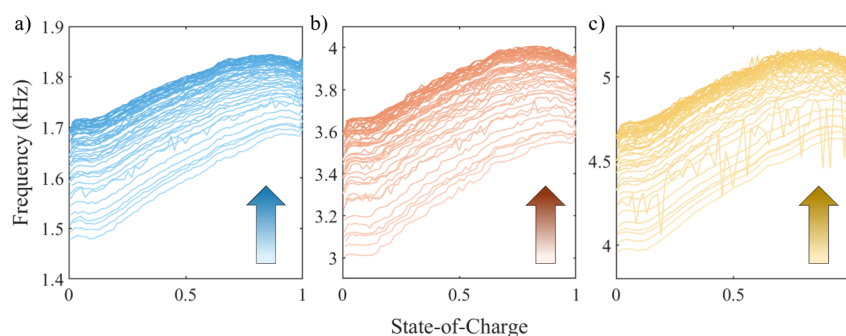
Figure 5. Three resonances as a function of SOC over 50 cycles at a $C/10$ rate. Light colors indicate early cycles while dark colors indicate later cycles. The frequency of the 1.6 kHz, 3.6 kHz, and 4.6 kHz resonances all initially increase before stabilizing to a certain frequency range.

dependence on the bulk mechanical properties of the LIB due to Li intercalation and deintercalation, as discussed previously.[2,11]

State-of-Charge and State-of-Health Tracking. To understand the dependance of the AIS spectra on the SOC over a long period, we conducted in-operando AIS over 50 cycles at $C/10$. Figure 5 shows the dependency of the frequency of each resonance as a function of the SOC of the battery. Light colors indicate early cycles, and dark colors indicate later cycles. To simplify the figure, only the discharge steps are shown. In individual cycles, trends identical to Figure 4 are seen. Over the long term, all three resonances initially increase in frequency before stabilizing to a certain frequency range, which suggests a stiffening of the cell independent of SOC. We note that, as a result of this drift, measured resonance frequencies are not unique to a certain SOC. A measured resonance frequency of 1.7 kHz may correspond to either 100% SOC on cycle 5 or 0% SOC on cycle 50. Thus, additional variables, mainly voltage, are needed to deconvolute these results.

This phenomenon, where LIBs tend to stiffen as they age, has been previously reported in UToF,[11] mechanical impedance experiments,[28] and compression testing.[29] However, the complexity of battery degradation makes it difficult to precisely identify the cause of aging. Most commonly, growth of the solid-electrolyte interface (SEI) layer is suggested as the root cause. Over time, the expansion and contraction of the graphite particles in the anode may fracture the SEI, promoting growth of this layer and causing the LIB to stiffen and swell. This theory is supported indirectly by measurements of the storage and loss moduli, dilatometry, and computational modeling.[28,30] For our purposes, we corroborate claims that extensive cycling results in cell stiffening. Similarly, the charge/discharge profiles of the cell (Figures S3a, b) show minimal impedance rise and some loss of capacity over the 50 cycles. This suggests that the primary degradation mechanism is Li inventory loss, possibly driven by SEI growth. However, while we concur that SEI growth is likely the cause of the cell stiffening, more work is needed to directly prove this claim.

For a quantitative measure of the correlation between the resonance frequency and the SOC, we turn to a correlation coefficient known as mutual information:[31]

$$I(X; Y) = \sum_{x \in X} \sum_{y \in Y} p(x, y) \log \frac{p(x, y)}{p(x)p(y)}$$

(5)

Where X and Y are the correlated functions, $p(x)$ and $p(y)$, are the probability mass functions of x, and $p(x, y)$ is the joint probability mass function of x and y. Mutual information quantifies the correlation between two functions, X and Y, without bias towards linearity, which is seen in other common correlation coefficients such as R^2. A full discussion of mutual information is given in the Supporting Information with comparisons to R^2. For the first cycle, the maximum possible mutual information occurs when SOC is correlated to itself, I (SOC, SOC). In this case, the mutual information is high, 3.3, which is expected since SOC is perfectly correlated with itself. When SOC is correlated with the voltage, I (SOC, V), the mutual information decreases to 1.65, which is still considered a strong correlation. When SOC is correlated with the resonance frequency, f_{res}, the mutual information is 1.64, 1.81, and 1.84 for the 1.6 kHz, 3.6 kHz, and 4.6 kHz resonances, respectively. Thus, we can extract as much information about SOC from the resonance frequencies as we can from the voltage. In a commercial BMS, AIS could be combined with voltage measurements to provide a more accurate SOC estimation.

Finally, we investigated mechanical changes in LIBs due to aging using in-operando AIS during a high-rate (1C), high temperature (45 °C) stress test, shown in Figure 6. All resonances decrease in frequency due to the temperature-dependent softening of the cell (Figure S3). Moreover, the 3.6 kHz resonance decreases in amplitude to the point where it is difficult to extract information below 50% SOC. Since the 3.6 kHz resonance follows the same trends as the 1.6 kHz and 4.6 kHz peaks, it is fully neglected. Even in these stressful conditions, AIS is able to effectively track mechanical changes in the LIB for hundreds of cycles.

The 1.6 kHz and 4.6 kHz peaks (Figure 6a, b) show some initial fluctuations before increasing significantly after 100 h, which corresponds to a stiffening of the cell. This process occurs faster than the 25 °C case due to the accelerated degradation of the LIB at high temperature and high rate. As with the room-temperature experiment, plotting the charge—discharge profiles show that capacity degradation is driven by Li loss with only a small increase in cell impedance during the experiment (Figure S3c, d). As before, we attribute this cell stiffening to SEI growth, though we note that more work is needed to directly prove this point.

As with SOC, we can apply mutual information to determine the correlation between SOH and f_{res}. Since SOH is only determined at 100% SOC, we extract f_{res} at 100% SOC for these calculations. First, we can determine the maximum I for this dataset: $I(\text{SOH, SOH}) = 4.09$. We then compare this with the I for the two identified resonances: $I(\text{SOH}, f_{1.6res}) = 1.50$; $I(\text{SOH}, f_{4.6res}) = 0.93$. Thus, the acoustic resonances can both
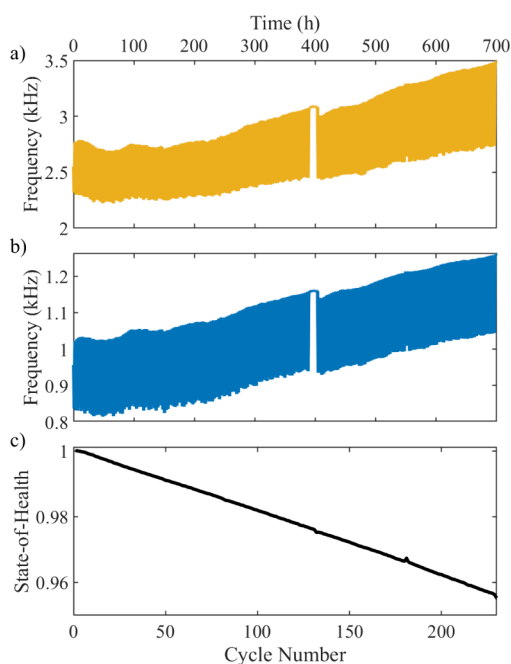
Figure 6. High temperature, high rate (45 °C, 1 C) degradation test. AIS is temperature-sensitive, causing all peaks to shift down in frequency. At high temperature, the acoustic damping increases such that the 3.6 kHz resonance is difficult to fit properly at certain SOCs. Therefore, this peak is neglected. Around 400 h, the cell cycler computer malfunctioned, leaving a short gap in the data. (a) The 4.6 kHz resonance and (b) the 1.6 kHz resonance, shifted to 2.5 kHz and 0.9 kHz, respectively. Over 700 h, these resonances increase significantly, suggesting a stiffening of the cell. (c) The SOH of the cell over the course of the experiment.

provide a significant quantity of information on SOH due to their relation to common degradation pathways such as excessive SEI growth or electrolyte consumption. This information would complement capacity and impedance data in a BMS, allowing for more accurate SOH predictions.

CONCLUSION

In this work, we have demonstrated the use of in-operando AIS to study the coupling between electrochemical reactions and the mechanical properties of commercial LIBs. AIS has the benefit of using small, inexpensive piezoelectric sensors and common instrumentation. Although the current work employed a $LiCoO_2$/graphite pouch cell, AIS is potentially suitable for different chemistries, such as $LiFePO_4$, and cell formats, such as D-cells, which are difficult to interrogate with UToF.[32] Using three acoustic resonances of the LIB, we show that in-operando AIS can effectively and repeatably track the mechanical changes that occur in LIBs during cycling. Using mutual information, we further showed that we can extract as much information about the SOC from the acoustic resonances as we can from the voltage. Finally, we showed that the acoustic resonances strongly correlate with the SOH of the LIB. This novel acoustic characterization technique is simple, inexpensive, and easy to implement, making it a good choice in both commercial and academic settings.

ASSOCIATED CONTENT

Supporting Information

The Supporting Information is available free of charge at https://pubs.acs.org/doi/10.1021/acselectrochem.4c00105.

A video showing the vibrational structure of the 1.6 kHz resonance (MP4)

A video showing the vibrational structure of the 3.6 kHz resonance (MP4)

A video showing the vibrational structure of the 4.6 kHz resonance (MP4)

Computational results and parameters, examples of different fitting equations, voltage profiles for Figures 5 and 6, temperature dependence of AIS, and a discussion of mutual information (PDF)

AUTHOR INFORMATION

Corresponding Author

Ping Liu − *Program of Materials Science and Engineering, University of California, San Diego, La Jolla, California 92093, United States; Aiiso Yufeng Li Department of Chemical and Nano Engineering, University of California, San Diego, La Jolla, California 92093, United States;* orcid.org/0000-0002-1488-1668; Email: piliu@ucsd.edu

Authors

Charles Soulen − *Program of Materials Science and Engineering, University of California, San Diego, La Jolla, California 92093, United States;* orcid.org/0000-0002-0752-614X

Stewart Sherrit − *Jet Propulsion Laboratory, California Institute of Technology, Pasadena, California 91109, United States*

Erik Brandon − *Jet Propulsion Laboratory, California Institute of Technology, Pasadena, California 91109, United States;* orcid.org/0000-0001-6106-7645

Complete contact information is available at:
https://pubs.acs.org/10.1021/acselectrochem.4c00105

Notes

The authors declare no competing financial interest.

REFERENCES

(1) Xu, R.; Zhao, K. Electrochemomechanics of Electrodes in Li-Ion Batteries: A Review. *J. Electrochem. Energy Convers. Storage* **2016**, *13* (3), 030803.

(2) Davies, G.; Knehr, K. W.; Van Tassell, B.; Hodson, T.; Biswas, S.; Hsieh, A. G.; Steingart, D. A. State of Charge and State of Health Estimation Using Electrochemical Acoustic Time of Flight Analysis. *J. Electrochem. Soc.* **2017**, *164* (12), A2746−A2755.

(3) Rieger, B.; Schlueter, S.; Erhard, S. V.; Schmalz, J.; Reinhart, G.; Jossen, A. Multi-Scale Investigation of Thickness Changes in a Commercial Pouch Type Lithium-Ion Battery. *J. Energy Storage* **2016**, *6*, 213−221.

(4) Hsieh, A. G.; Bhadra, S.; Hertzberg, B. J.; Gjeltema, P. J.; Goy, A.; Fleischer, J. W.; Steingart, D. A. Electrochemical-Acoustic Time of

Flight: In Operando Correlation of Physical Dynamics with Battery Charge and Health. *Energy Environ. Sci.* **2015**, *8* (5), 1569.

(5) Kazyak, E.; Wang, M. J.; Lee, K.; Yadavalli, S.; Sanchez, A. J.; Thouless, M. D.; Sakamoto, J.; Dasgupta, N. P. Understanding the Electro-Chemo-Mechanics of Li Plating in Anode-Free Solid-State Batteries with Operando 3D Microscopy. *Matter* **2022**, *5* (11), 3912−3934.

(6) Jiang, H.; Chen, J.; Li, X.; Jin, Z.; Chen, T.; Liu, J.; Li, D. A Comprehensive Review of In Situ Measurement Techniques for Evaluating the Electro-Chemo-Mechanical Behaviors of Battery Electrodes. *Molecules* **2024**, *29* (8), 1873.

(7) Lemarié, Q.; Alloin, F.; Thivel, P. X.; Idrissi, H.; Roué, L. Study of Sulfur-Based Electrodes by Operando Acoustic Emission. *Electrochimica Acta* **2019**, *299*, 415−422.

(8) Barai, P.; Mukherjee, P. P. Mechano-Electrochemical Model for Acoustic Emission Characterization in Intercalation Electrodes. *J. Electrochem. Soc.* **2014**, *161* (11), F3123−F3136.

(9) Bommier, C.; Chang, W.; Li, J.; Biswas, S.; Davies, G.; Nanda, J.; Steingart, D. Operando Acoustic Monitoring of SEI Formation and Long-Term Cycling in NMC/SiGr Composite Pouch Cells. *J. Electrochem. Soc.* **2020**, *167* (2), 020517.

(10) Chang, W.; Mohr, R.; Kim, A.; Raj, A.; Davies, G.; Denner, K.; Park, J. H.; Steingart, D. Measuring Effective Stiffness of Li-Ion Batteries *via* Acoustic Signal Processing. *J. Mater. Chem. A* **2020**, *8* (32), 16624−16635.

(11) Ladpli, P.; Kopsaftopoulos, F.; Chang, F. K. Estimating State of Charge and Health of Lithium-Ion Batteries with Guided Waves Using Built-in Piezoelectric Sensors/Actuators. *J. Power Sources* **2018**, *384*, 342−354.

(12) Din, E.; Schaef, C.; Moffat, K.; Stauth, J. T. A Scalable Active Battery Management System With Embedded Real-Time Electrochemical Impedance Spectroscopy. *IEEE Trans. Power Electron.* **2017**, *32* (7), 5688−5698.

(13) Sherrit, S.; Lee, H. J.; Bao, X.; Badescu, M.; Bar-Cohen, Y.; Harne, R. L. Composite Piezoelectric Resonator 1D Modeling with Loss. *Behavior and Mechanics of Multifunctional Materials IX* **2020**, 35.

(14) Meitzler, A. H.; O'Bryan, H. M.; Tiersten, H. F. Definition and Measurement of Radial Mode Coupling Factors in Piezoelectric Ceramic Materials with Large Variations in Poisson's Ratio. *IEEE Trans. Sonics Ultrason.* **1973**, *20* (3), 233−239.

(15) Sherrit, S.; Gauthier, N.; Wiederick, H. D.; Mukherjee, B. K. Accurate Evaluation of the Real and Imaginary Material Constants for a Piezoelectric Resonator in the Radial Mode. *Ferroelectrics* **1991**, *119* (1), 17−32.

(16) Leissa, A. *Vibration of Plates*; National Aeronautics and Space Administration: Washington D.C., 1969.

(17) Meng, K.; Chen, X.; Zhang, W.; Chang, W.; Xu, J. A Robust Ultrasonic Characterization Methodology for Lithium-Ion Batteries on Frequency-Domain Damping Analysis. *J. Power Sources* **2022**, *547*, 232003.

(18) Wang, H.; Kumar, A.; Simunovic, S.; Allu, S.; Kalnaus, S.; Turner, J. A.; Helmers, J. C.; Rules, E. T.; Winchester, C. S.; Gorney, P. Progressive Mechanical Indentation of Large-Format Li-Ion Cells. *J. Power Sources* **2017**, *341*, 156−164.

(19) Zheng, S.; Jiang, S.; Luo, Y.; Xu, B.; Hao, W. Guided Wave Imaging of Thin Lithium-Ion Pouch Cell Using Scanning Laser Doppler Vibrometer. *Ionics* **2021**, *27* (2), 643−650.

(20) Qi, Y.; Guo, H.; Hector, L. G.; Timmons, A. Threefold Increase in the Young's Modulus of Graphite Negative Electrode during Lithium Intercalation. *J. Electrochem. Soc.* **2010**, *157* (5), A558.

(21) Swallow, J. G.; Woodford, W. H.; McGrogan, F. P.; Ferralis, N.; Chiang, Y.-M.; Van Vliet, K. J. Effect of Electrochemical Charging on Elastoplastic Properties and Fracture Toughness of $Li_X CoO_2$. *J. Electrochem. Soc.* **2014**, *161* (11), F3084−F3090.

(22) Binpeng, Z.; Yan, L.; Jie, G.; Guorong, S.; Yung-chun, L.; Cunfu, H.; Weili, S.; Haosen, C. Ultrasonic Reflection/Transmission Characteristics for State of Charge of Li-Ion Battery. *Appl. Acoust.* **2023**, *214*, 109687.

(23) Pop, V.; Bergveld, H. J.; Notten, P. H. L.; Regtien, P. P. L. State-of-the-Art of Battery State-of-Charge Determination. *Meas. Sci. Technol.* **2005**, *16* (12), R93−R110.

(24) IEEE Standards Board. IEEE Standard on Piezoelectricity. *ANSIIEEE Std 176-1987* **1988**, DOI: 10.1109/IEEESTD.1988.79638.

(25) Sherrit, S.; Wiederick, H. D.; Mukherjee, B. K.; Sayer, M. An Accurate Equivalent Circuit for the Unloaded Piezoelectric Vibrator in the Thickness Mode. *J. Phys. Appl. Phys.* **1997**, *30* (16), 2354.

(26) Sherrit, S.; Olazabal, V.; Sansinena, J. M.; Bao, X.; Chang, Z.; Bar-Cohen, Y. The Use of Piezoelectric Resonators for the Characterization of Mechanical Properties of Polymers. *Smart Struct. Mater. 2002 Electroact. Polym. Actuators Devices EAPAD* **2002**, *4695* (35), 262−276.

(27) Berlincourt, D. A.; Curran, D. R.; Jaffe, H. Piezoelectric and Piezomagnetic Materials and Their Function in Transducers. In *Piezoelectric and Piezomagnetic Materials and Their Function in Transducers*; Elsevier, Inc., 1964; Vol. 1, pp 169−270.

(28) Von Kessel, O.; Deich, T.; Hahn, S.; Brauchle, F.; Vrankovic, D.; Soczka-Guth, T.; Birke, K. P. Mechanical Impedance as a Tool for Electromechanical Investigation and Equivalent Modeling of Lithium-Ion Batteries. *J. Power Sources* **2021**, *508*, 230337.

(29) Xu, J.; Jia, Y.; Liu, B.; Zhao, H.; Yu, H.; Li, J.; Yin, S. Coupling Effect of State-of-Health and State-of-Charge on the Mechanical Integrity of Lithium-Ion Batteries. *Exp. Mech.* **2018**, *58* (4), 633−643.

(30) Laresgoiti, I.; Käbitz, S.; Ecker, M.; Sauer, D. U. Modeling Mechanical Degradation in Lithium Ion Batteries during Cycling: Solid Electrolyte Interphase Fracture. *J. Power Sources* **2015**, *300*, 112−122.

(31) Cover, T. M.; Thomas, J. A. *Elements of Information Theory*, 1st ed.; Wiley, 2005. DOI: 10.1002/047174882X.

(32) Montoya-Bedoya, S.; Garcia-Tamayo, E.; Rohrbach, D.; Gaviria-Cardona, J. P.; Martinez-Tejada, H. V.; Planden, B.; Howey, D.; Florez, W. F.; Valencia, R. A.; Bernal, M. Quantitative Ultrasound Spectroscopy for Screening Cylindrical Lithium Ion Batteries for Second Life Applications. *Batter. Supercaps* **2024**, *7*, e202400002.